Performance Assessment of Fault Free Recursive ARAIM with High-Integrity Time-Correlated Measurement Error Models

Elisa Gallon, Samer Khanafseh, Boris Pervan, *Illinois Institute of Technology, Chicago, IL*
Mathieu Joerger, *Virginia Tech, Blacksburg, VA*

BIOGRAPHY

Elisa Gallon received her Bachelor's Degree in Mathematics from Université Blaise Pascal, France in 2014 and her Master of Science in Global Navigation Satellite Systems from ENAC and ISAE-Supaéro in 2016. From 2016 to 2017, she worked at the European Space Agency (ESA) on Orbit Determination and Time Synchronization of Galileo satellites. She is currently a Ph.D. Candidate at the Navigation Laboratory in the Department of Mechanical and Aerospace Engineering at Illinois Institute of Technology (IIT) in Chicago.

Dr. Samer Khanafseh is currently a Research Associate Professor at Mechanical and Aerospace Engineering Department at IIT. He received his M.S. and Ph.D. degrees in Aerospace Engineering from IIT, in 2003 and 2008, respectively. Dr. Khanafseh has been involved in several aviation applications such as Autonomous Airborne Refueling (AAR) of unmanned air vehicles, autonomous shipboard landing for NUCAS and JPALS programs and Ground Based Augmentation System (GBAS). He published 13 journal articles and more than 30 conference papers. His research interests are focused on high accuracy and high integrity navigation algorithms for close proximity applications, cycle ambiguity resolution, high integrity applications, fault monitoring and robust estimation techniques. He was the recipient of the 2011 Institute of Navigation Early Achievement Award for his outstanding contributions to the integrity of carrier phase navigation systems.

Dr. Mathieu Joerger obtained a Master in Mechatronics from the National Institute of Applied Sciences in Strasbourg, France, in 2002. He earned a M.S. in 2002 and a Ph.D. in 2009 in Mechanical and Aerospace Engineering at IIT in Chicago. He is the 2009 recipient of the Institute of Navigation (ION) Bradford Parkinson award, and the 2014 recipient of the (ION) Early Achievement Award. He is also an Associate Editor of Navigation for the Institute of Electrical and Electronics Engineers (IEEE) Transactions on Aerospace and Electronic Systems. Dr. Joerger is currently assistant professor at Virginia Tech, in Blacksburg, VA, working on multi-sensor integration for safe navigation and collision warning of automated driving systems (ADS). He is a member of the E.U./U.S. Advanced RAIM (ARAIM) Working Group C.

Dr. Boris Pervan is a Professor of Mechanical and Aerospace Engineering at the Illinois Institute of Technology (IIT), where he conducts research on high integrity navigation systems. Prior to joining the faculty at IIT, he was a spacecraft mission analyst at Hughes Aircraft Company (now Boeing) and a postdoctoral research associate at Stanford University. Prof. Pervan received his B.S. from the University of Notre Dame, M.S. from the California Institute of Technology, and Ph.D. from Stanford University. He has received the IIT Sigma Xi Excellence in University Research Award (twice), IIT University Excellence in Teaching Award, IEEE Aerospace and Electronic Systems Society M. Barry Carlton Award, RTCA William E. Jackson Award, Guggenheim Fellowship (Caltech), and the Albert J. Zahm Prize in Aeronautics (Notre Dame). He is a Fellow of the Institute of Navigation (ION) and former Editor-in-Chief of the ION journal NAVIGATION.

ABSTRACT

In this paper, we develop a new Kalman-filter (KF)-based approach for Global Navigation Satellite Systems (GNSS) positioning, fault detection, and integrity monitoring. The filter design integrates stochastic measurement error models developed and validated in prior work using multiple years of data (Gallon et al., 2020, 2021, 2022). These models account for uncertain measurement error time-correlation using power spectral density (PSD) bounding (Langel et al., 2020). They are used in this paper to provide a realistic performance assessment of recursively-implemented Advanced Receiver Autonomous Integrity Monitoring (ARAIM).

I. INTRODUCTION

The modernization of GPS and the deployment of additional GNSS constellations have increased the number of redundant ranging signals, leading to heightened interest in the development of ARAIM for aircraft navigation. The baseline version of ARAIM uses ionosphere-free carrier smoothed code (CSC) measurements at one instant in time to provide a "snapshot"

navigation solution (Working Group C, 2012, 2014, 2016). Unlike conventional snapshot ARAIM, a recursive implementation of ARAIM is able to exploit changes in satellite geometry. The accumulated geometry variations of redundant satellites from multiple GNSS can be substantial. In Joerger and Pervan (2020), we showed that the additional exploitation of satellite motion over time could provide superior positioning performance and tighter protection levels (PLs) than baseline ARAIM. Recursive algorithms can therefore open the possibility to extend the scope of ARAIM applications beyond aircraft navigation, to rail, maritime/naval, or arctic operations.

Additionally, GNSS can provide continuous worldwide absolute positioning but requires visibility of four or more satellites, which is not always achievable in sky-obstructed environments. Also, GNSS is vulnerable to radio-frequency interference. In contrast, inertial sensors are not directly impacted by these external factors. Inertial Navigation Systems (INS) can be used as dead reckoning sensors to estimate displacements over time, but state estimation errors drift due to the temporal integration of IMU errors. Combining INS and GNSS using a Kalman filter (KF) can simultaneously limit the drift in INS positioning error and provide continuity through sky obstructions and robustness against GNSS jamming and spoofing attacks Tanil et al. (2018). GNSS/INS integration is accomplished through measurement filtering, which requires robust modeling of stochastic errors *over time* to ensure navigation integrity.

To implement either of these two applications, one must ensure that the error models implemented in the KF properly account for time correlation. In both applications, dynamic models for the three main error sources affecting ionosphere-free GNSS signals are needed: orbit and clock errors, tropospheric delay, and multipath.

Building on the prior work of DeCleene (2000) and Rife et al. (2006), Perea (2019) employed over-bounding theory to define upper bounds on the variances of orbit and clock errors for both GPS and Galileo satellites. These error models are sufficient for snapshot positioning, but not for time-sequential implementations because they do not address the stochastic dynamics of the errors over time.

Langel (2014) derived an analytical bound on integrity risk for time-sequential linear estimators using Autocorrelation Function (ACF) bounding. We used experimental data to evaluate ACF bounds for GPS and Galileo orbit and clock errors in Gallon et al. (2019). But, Langel's ACF-based approach requires continuous, cumulative storage of all data and estimator coefficients over time, and except for short, finite-horizon intervals, is unsuitable for KF implementations. More recently, Langel et al. (2020) introduced the concept of Power Spectral Density (PSD) bounding. The PSD bounding method, unlike ACF bounding, is not restricted to fixed-interval implementations and is compatible with Kalman filtering.

In prior work (Gallon et al., 2020, 2021, 2022), multiple years of data were processed to derive bounding, time-correlated error models for GNSS error sources via the PSD bounding method.

The first part of this paper outlines the specifics of our recursive ARAIM implementation. In particular, two aspects are highlighted:

- Unlike snapshot ARAIM, which relies on dual-frequency, ionospheric-free carrier-smoothed-code measurements, recursive ARAIM mainly uses raw carrier phase measurements. Dual-frequency code phase measurement errors will be heavily influenced by antenna group delays, the dynamics of which cannot be modelled stochastically in a KF. Indeed, antenna group delays are deterministic processes: the errors will change according to the antenna's environment, as well as substantial platform reorientations (e.g., turns, banks) and satellite line of sight variation. In principle, this effect is calibratable, albeit not always easily for many platforms of interest, like civil transport aircraft. Although much the same can be said for multipath, in this case error dynamics are highly sensitive to small scale attitude motions and further complicated by a multiplicity of reflective surfaces on platforms with complex shapes, (again) like transport aircraft, making multipath far more amenable to stochastic modelling. We focus on raw carrier phase measurements because their platform/antenna dependent errors are restricted to multipath and thermal noise, which can be modelled stochastically in a KF. Code measurements are used to aid in the initialization of floating carrier cycle ambiguities, but they will not otherwise be used (or needed) in the recursive ARAIM KF.
- To properly account for the time correlation of the errors present in the raw carrier measurements (satellite orbit and clock, residual tropospheric error, multipath, and thermal noise), bounding dynamic error models derived in our prior work (Gallon et al., 2020, 2021, 2022) are used in this work. These bounding models are first order Gauss-Markov processes incorporated into the KF by state augmentation.

The second half of this paper assesses the performance improvements provided by recursive ARAIM, using bounding dynamic error models, with respect to baseline snapshot ARAIM, using baseline snapshot models. Additionally, a sensitivity analysis is performed on each of the error model parameters to assess which of them impacts the KF performance (i.e. covariance) the most.

II. INTEGRITY THROUGH POWER SPECTRAL DENSITY BOUNDING

This section offers insights into the benefits of PSD bounding when it comes to guarantying integrity.

Let us consider the simple case of a steady-state KF fed by zero-mean, stationary sensor and process noise contributions with known PSDs. Because the KF is a linear filter, each independent error source can be evaluated separately and the results can be added after.

Consider a scalar error input $x(t)$ with PSD $S_{xx}(f)$. The KF transfer function from $x(t)$ to some scalar output of interest $y(t)$ is $H(f)$. The KF is designed using $S_{xx}(f)$. The mean of the KF output error is zero (because the input is zero-mean), and the output error variance is:

$$\sigma_y^2 = \int_{-\infty}^{\infty} |H(f)|^2 S_{xx}(f) df, \tag{1}$$

Now suppose that the actual input is $\underline{x}(t)$, where $S_{\underline{x}\underline{x}}(f) < S_{xx}(f) \ \forall -\infty \leq f \leq \infty$, and the actual output is $\underline{y}(t)$. The KF, designed using $S_{xx}(f)$, will produce a predicted output error variance that remains unchanged, i.e. σ_y^2. But the actual output error variance will be $\sigma_{\underline{y}}^2$. It is obvious from Equation (1) that $\sigma_{\underline{y}}^2 < \sigma_y^2$.

In prior work Gallon et al. (2021), we showed that this simple derivation could also be applied to more complex cases (e.g. time varying KF). In other words, we showed that the upper bounding of the measurement errors' PSDs ensured an upper bound for the estimation error variance.

The new error models used in this work have been derived/analyzed extensively in prior work (Gallon et al., 2020, 2021, 2022) based on this concept of PSD bounding (Langel et al., 2020). The three main GNSS errors impacting our measurements—orbit and clock errors, multipath, and tropospheric delay—are modeled using First Order Gauss Markov Random Processes (FOGMRP). The following section goes into more details on how each GNSS error model was obtained.

III. GNSS ERROR MODELS

The Kalman filter derived in this work relies on two types of measurements: iono-free code and carrier measurements. As the signal travels between the satellite and the user, it is impacted by satellite orbit and clock errors, tropospheric delay, multipath and thermal noise. In order for the KF estimation variance to be bounding, these errors must be modeled and accounted for properly. This section describes each error term impacting measurements, and summarises how their models were developed in prior work.

1. Measurements of Interest

The iono-free code and carrier measurements of satellite i at epoch k can respectively be expressed as:

$$\rho_k^i = r_k^i + c\left(dt_{r,k} - dt_k^i\right) + m_t(\theta_k^i)T_k + m_{MP}(\theta_k^i)\varepsilon_{MP,\rho,k}^i + \varepsilon_{TN,\rho,k}^i \tag{2}$$

$$\phi_k^i = r_k^i + c\left(dt_{r,k} - dt_k^i\right) + \eta_{IF}^i + m_t(\theta_k^i)T_k + m_{MP}(\theta_k^i)\varepsilon_{MP,\phi,k}^i + \varepsilon_{TN,\phi,k}^i \tag{3}$$

where r_k^i is the satellite-to-receiver range, c is the speed of light, dt^i is the satellite clock bias, $dt_{r,k}$ is the receiver clock bias, $m_t(\theta_k^i)$ and $m_{MP}(\theta_k^i)$ are the elevation (θ) dependent mapping functions of the tropospheric delay and multipath error respectively, T_k is the zenith tropospheric delay, $\varepsilon_{MP,\rho,k}^i$ and $\varepsilon_{MP,\phi,k}^i$ are the code and carrier multipath errors, $\varepsilon_{TN,\rho,k}^i$ and $\varepsilon_{TN,\phi,k}^i$ are the code and carrier thermal noises, and η_{IF}^i is the satellite-dependent constant floating carrier cycle ambiguity.

The ARAIM algorithm (Working Group C, 2012, 2014, 2016) relies on carrier smoothed code: the noisy (but unambiguous) code pseudorange measurements are smoothed with the precise (but ambiguous) carrier phase measurements.

But dual frequency code measurements are heavily impacted by antenna group delays. Their dynamics are deterministic but depend on the antenna type and antenna environment. Calibrating those group delays are in principle possible, but cumbersome since they depend on antenna brand and model, and are sensitive to small-scale aircraft motions. Therefore, we focus on raw carrier phase measurements, because their platform/antenna dependant errors are dominated by multipath and thermal noise, unlike code measurements. Code measurements will only be used at the first epoch of a satellite's visibility, to initialize floating carrier cycle ambiguities.

Iono-free carrier (and code) measurements are impacted by 3 sources of time-correlated errors: orbit and clock errors, tropospheric delay, and multipath. These errors have all been modeled as FOGMRP, because these processes' time-correlated

Table 1: GNSS Error Model FOGMRP Parameter Values

Error Type	Clocks	Time Constant [sec]	Standard Deviation [m]
Orbit and Clock	GPS	18000	1.8
	GAL	7200	0.65
Troposphere	/	72000	0.09
Carrier phase multipath	/	200	0.028

models are "KF friendly". The associated error models used in this work are described in the following subsections and summarized in Table 1.

The dynamics of a FOGMRP, with parameters σ & τ, are expressed in discrete form as:

$$x_{k+1} = e^{-\Delta t/\tau} x_k + \sqrt{\sigma^2 \left(1 - e^{-2\Delta t/\tau}\right)} \omega_k, \qquad \omega_k \sim N(0,1) \quad \text{and} \quad x_0 \sim N\left(0, \sigma_0^2\right) \tag{4}$$

where σ_0^2 is the initial variance of the process (more details in Section V.3).

The following subsection briefly describes each of the error components, as well as the method used in prior work to develop corresponding bounding, time correlated error models to be used in this work.

2. Orbit and Clock Errors

In Gallon et al. (2020, 2022), satellite clock, orbit radial, cross and along track errors for GPS and Galileo were processed over a three year period (2018-2020). Three scenarios were considered as a good representation of user orbit and clock errors:

- Case 1: the user on earth is located at the closest distance from the satellite (i.e. nadir).
- Cases 2 & 3: the user on earth is located at the farthest distance from the satellite (i.e. horizon).

These cases encompass worst case scenarios for earth users. While, analysing the errors over those 3 years, we showed that the orbit and clock errors could be modeled as zero mean (yearly mean error values were close to zero). Additionally, because GPS and Galileo errors are so different, their errors were modeled separately (i.e. two different models were developed).

We used PSD bounding methods to account for GPS satellite errors and used a FOGRMP model with parameters are $\sigma_{GPS} = 1.8$m and $\tau_{GPS} = 5$h. Similarly, Galileo errors are modeled as $\sigma_{GAL} = 0.65$m and $\tau_{GAL} = 2$h. For simplicity, those parameters will be referred to as σ_{orb} and τ_{orb}.

3. Tropospheric Delay

In Gallon et al. (2021), tropospheric delays were analyzed for the year 2018 at 100 locations worldwide. Two tropospheric models were evaluated and their residuals were modeled as FOGMRP. In this work, we will rely on the GPT2w error model (Boehm et al., 2014) to estimate the tropospheric delays, because Gallon et al. (2021) showed that its residuals were small and unbiased globally (simpler to model).

Let us express the *slant* tropospheric delay in terms of its hydrostatic (dry, noted $T_{D,k}$) and non-hydrostatic (wet, noted $T_{W,k}$) components:

$$T_k = T_{W,k} + T_{D,k} \tag{5}$$

The slant delays can be related to the vertical delays (Zenith Tropospheric Delay - ZTD) via a dry and a wet deterministic mapping functions. In this work, the VMF1 (Vienna Mapping Functions 1) m_W and m_D for the wet and dry ZTP components ($T_{W,k}^{ZTD}$ and $T_{D,k}^{ZTD}$) are used (Boehm et al., 2014):

$$T_k = T_{W,k}^{ZTD} m_W(\theta_k^i) + T_{D,k}^{ZTD} m_D(\theta_k^i) \tag{6}$$

The GPT2w model estimates the wet and dry ZTD separately (noted $T^{ZTD}_{W,GPT2w,k}$ and $T^{ZTD}_{D,GPT2w,k}$), with residual errors noted $\delta T^{ZTD}_{W,GPT2w,k}$ and $\delta T^{ZTD}_{D,GPT2w,k}$:

$$T_k = \left(T^{ZTD}_{W,GPT2w,k} + \delta T^{ZTD}_{W,GPT2w,k}\right) m_W(\theta^i_k) + \left(T^{ZTD}_{D,GPT2w,k} + \delta T^{ZTD}_{D,GPT2w,k}\right) m_D(\theta^i_k) \tag{7}$$

In prior work (Gallon et al., 2021), we modeled the post-GPT2w-model residuals without distinction between the wet and dry components. Since the wet component varies faster and more randomly than the hydrostatic component, it is safe to assume that most of the residuals estimated in Gallon et al. (2021) are wet residuals. Therefore, in this work, the tropospheric delay will be assumed to have the following expression:

$$\begin{aligned} T_k &= \left(T^{ZTD}_{W,GPT2w,k} + \Delta T_k\right) m_W(\theta^i_k) + T^{ZTD}_{D,GPT2w,k} m_D(\theta^i_k) \\ &= T_{GPT2w,k} + \Delta T_k m_W(\theta^i_k) \end{aligned} \tag{8}$$

$T^{ZTD}_{W,GPT2w,k}$ is the total vertical tropo delay etimated by the GPT2w model. A FOGMRP is used to upper bound the zenith delay residuals of the wet tropospheric residuals ΔT_k, and its parameters (σ_{trop} and τ_{trop}) are shown in Table 1.

4. Multipath

The multipath model used in this work has been derived from data collected on the rooftop of the Illinois Institute of Technology Retalliata Engineering building, in Chicago IL. The experimental KF estimation performance assessment in the following sections will use data from the same antenna.

Multipath error $\varepsilon_{MP,\phi}$ is modeled as a product of two main components: a deterministic component, which depends on satellite elevation (θ^i), and a random component, which depends on the environment of the receiver:

$$\varepsilon^i_{MP,\phi,k} = m_\phi(\theta^i)\epsilon_{MP,\phi,k} \tag{9}$$

The deterministic component (called a mapping function $m_\phi(\theta^i)$ is expressed as:

$$m_\phi(\theta^i) = \sqrt{\frac{f^4_{L1} + f^4_{L2}}{\left(f^2_{L1} - f^2_{L2}\right)^2}} \left(1 + 2.9e^{-\theta^i/10}\right), \tag{10}$$

where θ^i is the elevation of satellite i (in degrees), and f_{L1} and f_{L2} are the (constellation dependent) transmitting frequencies (L1 and L2 for GPS, E1 and E5a for Galileo).

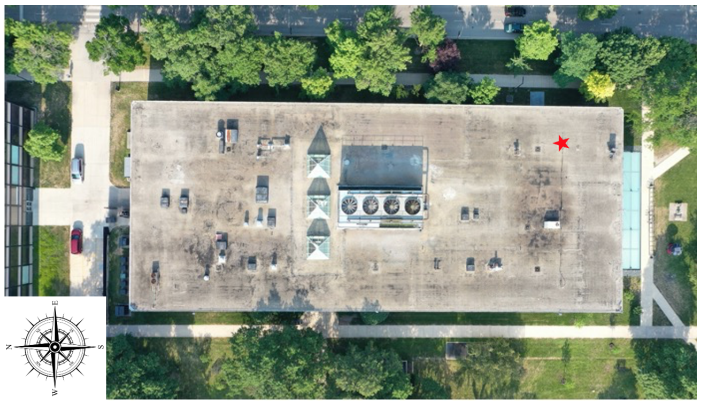

Figure 1: Multipath environment

The random component ($\epsilon_{MP,\phi}$) is modeled separately and is propagated in the KF time update. A detailed analysis of multipath errors was performed but is not included here to limit the length of this paper. In this analysis, we evaluated carrier phase measurement errors due to multipath using L1 − L2 carrier phase data collected at the location shown in Figure 1. We used this data to determine that the single-frequency carrier-phase multipath errors could be robustly modeled (i.e., PSD-upper-bounded) using a FOGMRP with $\sigma_\phi = 2.8$ cm and $\tau_\phi = 200$ sec.

Code measurements are used at the first epoch of visibility of a satellite to help in the initialization of the satellite's cycle ambiguity. The multipath on raw code measurements at low elevation is modeled as (the derivation of this model is not included to limit the length of this paper):

$$\epsilon_{MP,\rho} \sim N\left(0, \frac{f_{L1}^4 + f_{L2}^4}{\left(f_{L1}^2 - f_{L2}^2\right)^2}\sigma_\rho^2\right), \tag{11}$$

where σ_ρ is a function of the satellite's elevation (in degrees) and is expressed as:

$$\sigma_\rho(\theta^i) = P_\rho(1)\left(\theta^i\right)^3 + P_\rho(2)\left(\theta^i\right)^2 + P_\rho(3)\theta^i + P_\rho(4), \tag{12}$$

where $P_\rho = \left[-3.865e^{-6}, 3.550e^{-4}, -7.559e^{-3}, 0.6423\right]$.

Similarly, the carrier smoothed code snapshot multipath model (used in the Least Square approach of Section V.2) is modeled with the polynomial $P_{\tilde{\rho}} = \left[-3.81e^{-6}, 6.155e^{-4}, -0.0325, 0.749\right]$.

5. Receiver Noise

The receiver noise of the carrier smoothed code of satellite i at epoch k is modeled as a zero mean white Gaussian noise:

$$\sigma_{TN,\tilde{\rho},i,k} = \sqrt{\frac{f_{L1}^4 + f_{L2}^4}{\left(f_{L1}^2 - f_{L2}^2\right)^2}}\left(0.15 + 0.43e^{-\theta^i/6.9}\right) \tag{13}$$

The carrier phase thermal noise $\varepsilon_{TN,\phi,k}$ is modeled as white Gaussian noise whose variance is related to its carrier-smoothed-code counterpart by the equation (Joerger and Pervan, 2020):

$$\sigma_{TN,\phi,i,k} = 0.196\ \ \sigma_{TN,\tilde{\rho},i,k} \tag{14}$$

IV. KALMAN FILTER DESIGN

The following sections describe the steps employed in this work for KF design:

1. System State Selection

In previous sections, we introduced new, time correlated, upper bounding error models for each of the error terms impacting the GNSS signals. These error models are FOGMRP, i.e. colored noise. To incorporate them in a KF, we can use state augmentation. Considering the following state vector:

$$\mathbf{x}_k = \begin{bmatrix}\mathbf{r}_{3\times1} & \mathbf{b}_{2\times1} & \boldsymbol{\epsilon}_{MP_{\Phi}n\times1} & \Delta T_{1\times1} & \boldsymbol{\eta}_{IF_{n\times1}} & \boldsymbol{\Delta S}_{n\times1}\end{bmatrix}^T \tag{15}$$

where n is the total number of satellites in view at time k, $\mathbf{r}$ is the 3D ENU position estimate of the receiver, $\mathbf{b}$ are the user clock biases for the GPS and Galileo constellations, $\boldsymbol{\epsilon}^i_{MP,\phi,k}$ are the carrier multipath errors, ΔT is the GPT2w zenith tropospheric delay residual, $\boldsymbol{\eta}_{IF}$ is the iono-free carrier phase ambiguity and $\boldsymbol{\Delta S}$ are the satellite orbit and clock residual errors.

Given n satellites in view at time k, the state vector $\mathbf{x}_k$ will have a dimension of $N_{KF} = 3n + 6$ and the measurement vector will have a dimension of $N_{meas} = n$.

2. System Dynamic Model

The system's discrete dynamic model is as follows:

$$\mathbf{x}_{k+1} = \mathbf{\Phi}_k \mathbf{x}_k + \mathbf{\Gamma}_k w_k \tag{16}$$

where $\mathbf{x}_k$ is the state vector described in Section IV.1, $\mathbf{\Gamma}_k$ maps the process noise input matrix, and the state transition matrix $\mathbf{\Phi}_k$ and process noise covariance matrix $\mathbf{W}_k$ are expressed as:

$$\mathbf{\Phi}_k = \begin{bmatrix} \mathbf{I}_{3\times3} & & & & & & \\ & \mathbf{I}_{2\times2} & & & & & \\ & & e^{-\Delta t/\tau_\phi}\mathbf{I}_{n\times n} & & & & \\ & & & e^{-\Delta t/\tau_{trop}} & & & \\ & & & & \mathbf{I}_{n\times n} & & \\ & & & & & e^{-\Delta t/\tau_{orb}}\mathbf{I}_{n\times n} & \end{bmatrix},$$

$$\mathbf{W}_k = \begin{bmatrix} w_\infty \mathbf{I}_{3\times1} & & & & & & \\ & w_\infty \mathbf{I}_{2\times1} & & & & & \\ & & \sigma_\phi^2\left(1-e^{-2\Delta t/\tau_\phi}\right)\mathbf{1}_{n\times1} & & & & \\ & & & \sigma_{trop}^2\left(1-e^{-2\Delta t/\tau_{trop}}\right) & & & \\ & & & & \mathbf{0}_{n\times1} & & \\ & & & & & \sigma_{orb}^2\left(1-e^{-2\Delta t/\tau_{orb}}\right)\mathbf{1}_{n\times1} & \end{bmatrix},$$

where $\mathbf{I}$ is the identity matrix, and w_∞ is an arbitrarily large value.

The diagonal components of the augmented states follow the dynamic's of a FOGMRP introduced earlier in Equation 4. Since the user's trajectory is not pre-defined, our knowledge of the position and clock dynamics is assumed to be null (large process noise).

3. Measurement Model

The measurements are iono-free code and carrier measurements. Code measurements are only used at the first epoch a satellite is visible, whereas carrier phase measurements are continuously used to estimate the state vector. The measurement model can therefore be expressed as:

$$\mathbf{z}_k = \mathbf{H}_k \mathbf{x}_k + \boldsymbol{\nu}_k \tag{17}$$

where $\mathbf{z}_k = \begin{bmatrix}\delta\phi_k^1 & \dots & \delta\phi_k^n\end{bmatrix}^T$, and $\delta\phi_{\mathbf{k}}^{\mathbf{i}}$ are the carrier measurements after corrections (GPT2w and satellite clock), $\boldsymbol{\nu}_k$ is the measurement noise vector, such that $\boldsymbol{\nu}_k \sim \mathcal{N}(\mathbf{0}, \mathbf{V}_k)$, and the observation matrix $\mathbf{H}_k$ and measurement error covariance matrix $\mathbf{V}_k$ are defined as:

$$\mathbf{H}_k = \begin{bmatrix} \mathbf{G}_{kn\times3} & \begin{matrix}\mathbf{1}_{n_{GPS}\times1}\\ \mathbf{0}_{n_{GAL}\times1}\end{matrix} & \begin{matrix}\mathbf{0}_{n_{GPS}\times1}\\ \mathbf{1}_{n_{GAL}\times1}\end{matrix} & m_\phi\mathbf{I}_{n\times n} & m_{W\,n\times1} & \mathbf{I}_{n\times n} & \mathbf{I}_{n\times n} \end{bmatrix},$$

and

$$\mathbf{V}_k = \begin{bmatrix} \sigma_{TN,\phi,1,k}^2 & & \\ & \ddots & \\ & & \sigma_{TN,\phi,n,k}^2 \end{bmatrix}.$$

The measurement errors contained in $\boldsymbol{\nu}_k$ are comprised of the thermal noise, all the other error terms are being handled by state augmentation.

4. KF Equations and Initialization

The KF relies on the successive use of two equations: the time update (prediction) and the measurement update.

The time update relies on the user's knowledge of the errors' dynamics. At any epoch k, the state vector and covariance matrices are updated using the following equations:

$$\mathbf{x}_{k|k-1} = \mathbf{\Phi}_k \mathbf{x}_{k-1|k-1}, \tag{18}$$

$$\mathbf{P}_{k|k-1} = \mathbf{\Phi}_k \mathbf{P}_{k-1|k-1} \mathbf{\Phi}_k^T + \mathbf{\Gamma}_k \mathbf{W}_k \mathbf{\Gamma}_k^T. \tag{19}$$

The measurement update can be expressed as:

$$\mathbf{x}_{k|k} = \mathbf{x}_{k|k-1} + \mathbf{L}_k \left(\mathbf{z}_k - \mathbf{H}_k \mathbf{x}_{k|k-1} \right), \tag{20}$$

$$\mathbf{P}_{k|k} = \left(\mathbf{I}_{n\times n} - \mathbf{L}_k \mathbf{H}_k \right) \mathbf{P}_{k|k-1}, \tag{21}$$

where $\mathbf{L}_k = \mathbf{P}_{k|k-1}\mathbf{H}_k^T \left(\mathbf{V}_k + \mathbf{H}_k \mathbf{P}_{k|k-1} \mathbf{H}_k^T \right)^{-1}$ is the Kalman gain.

Finally, the state vector estimate is initialized using the following expression:

$$\mathbf{x}_0 = \begin{bmatrix} \mathbf{0}_{1\times 3} & \mathbf{0}_{1\times 2} & \mathbf{0}_{1\times n} & 0 & (\delta\boldsymbol{\phi}_k - \delta\boldsymbol{\rho}_k)_{1\times n} & \mathbf{0}_{1\times n} \end{bmatrix}^T, \tag{22}$$

where $\delta\boldsymbol{\rho}_k$ and $\delta\boldsymbol{\phi}_k$ are the code and carrier measurements of the new satellites in view, after corrections (GPT2w and satellite clock).

And the covariance matrix is initialized as the following matrix:

$$\mathbf{P}_0 = \begin{bmatrix} w_\infty \mathbf{I}_{3\times 3} & & & & & \\ & w_\infty \mathbf{I}_{2\times 2} & & & & \\ & & \sigma_\phi^2 \mathbf{I}_{n\times n} & & & \\ & & & \sigma_{trop}^2 & & \\ & & & & \alpha\sigma_\rho^2 \mathbf{I}_{n\times n} & \\ & & & & & \sigma_{orb}^2 \mathbf{I}_{n\times n} \end{bmatrix}, \tag{23}$$

where the inflation factor α accounts for the unknown/un-modeled impact of the group delay on the code measurements and its effect on the initial estimate of the ambiguity.

Note that position and clock states are given very high initial covariance values (w_∞) because we do not assume prior knowledge on these states, cycle ambiguity states are initialized based on the code measurement noise, and that the other states are initialized based on their steady states values.

V. PERFORMANCE ASSESSMENT

In this section, we assess two key elements of this research:

- The value of a Kalman Filtering (KF) approach over the (more traditional) Least Squares Estimator (LSE) method. Assuming that both methods are given the same error models, what are the performance benefits of a KF over a LSE approach?
- The sensitivity of our KF to the error models derived in Section III.

To address these two points, we collected and processed data described in the following subsection.

1. Experimental set up

On September 5th 2022, 24 hours of data were collected at a 1 sec sampling rate using a OEM6 NovAtel receiver and pinwheel NovAtel antenna, located on the rooftop of the Retalliata Engineering building (Illinois Institute of Technology campus). The environment of the antenna is in Figure 1, where the red star represents the antenna location.

These 24h are divided into six 4h segments. The first 4h segment is used in subsections V.2, V.3 , V.4 and V.5. The other segments are also used for validation in subsection V.5.

Because the orbit and clock error models derived in Gallon et al. (2020, 2022) are restricted to the GPS and Galileo constellations, only those two constellations were processed in this paper. The number of visible GPS & Galileo satellites during the experiment is represented in Figure 2. Note that all of the following subsections are assuming a fault-free scenario.

2. Case A: Advantage of KF over LSE with the same error models

In this first test case, we evaluate the performance improvement of a KF incorporating time correlated error models over the LSE approach. The error models standard deviations, coefficients and mapping functions described in Section III are applied to both the LSE and KF approaches. Since LSE is a snapshot approach, the time constants in Table 1 are not involved in the

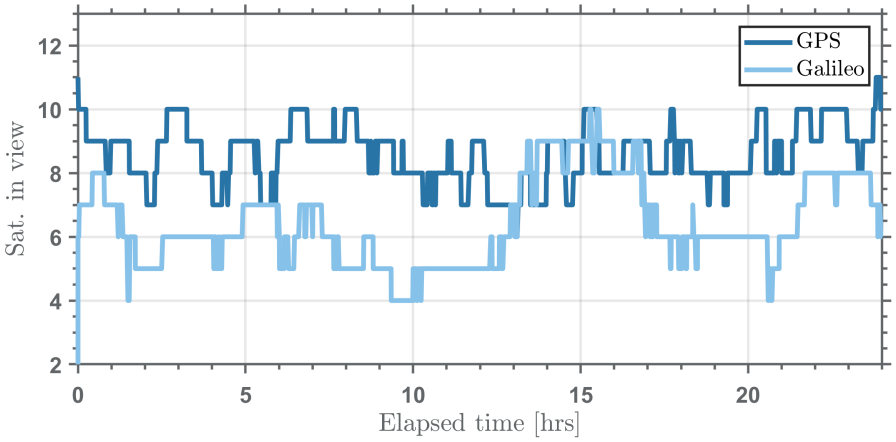

Figure 2: GPS and Galileo satellites in view

estimation process. The LSE uses carrier-smoothed-code measurements, whereas the KF only uses code during the first epoch of a satellite in view. For a fair covariance comparison between the LSE and the KF performance, we assume $\alpha = 1$ in Equation 23 (a different value of alpha will be used in Section V.5).

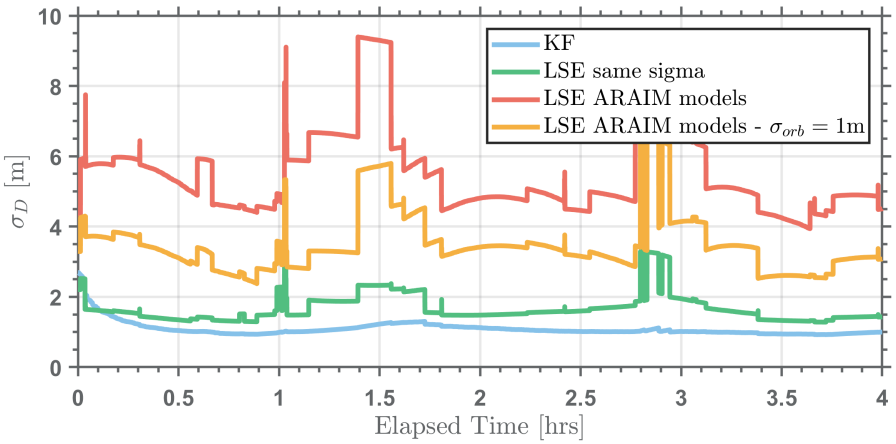

Figure 3: Covariance results for the down direction

Figure 3 shows the vertical position error standard deviation curves obtained over a 4h window, for both the LSE (green curve) and the KF (blue curve) systems. Because the Kalman filter relies on code measurements to initialize the cycle ambiguities impacting the carrier measurements, and because raw code measurements have a larger variance than carrier smoothed code (used in the LSE), the KF starts off with a slightly larger covariance during the first few minutes. Overall, the KF provides a smaller and smoother covariance envelope than that of the LSE, with an asymptotic values at the meter level. One can also note that the KF is not as impacted by satellites coming in and out of view, unlike the LSE, for instance at $t = 2.8$h, which sees variations in the meter level.

3. Case B: Advantage of KF with time correlated bounding models over Fault free LSE ARAIM

In this subsection, we compare the results obtained from 3 estimation processes:

- KF with time correlated, bounding error models (as described in Section III), blue curve,
- LSE with the ARAIM error models (Working Group C, 2012, 2014, 2016), red curve,
- LSE with the ARAIM error models, but $\sigma_{orb} = 1$ m, orange curve.

These 3 different scenarios allow us to observe the performance improvements (in terms of covariance) for an ARAIM user to

switch from LSE to KF, as well as analyse the impact of the orbital error models on the current ARAIM algorithm.

Let us first compare the performance of the KF (as described in Section IV, with the error models presented in Section III) compared to that of a LSE with the error models used in FF ARAIM (Working Group C, 2012, 2014, 2016).

In Figure 3, unlike the KF results (in light blue), the LSE results (red curve) have a mean value of approximately 5 meters and are varying greatly as satellite go in and out of view, and as geometry changes, with variations reaching sometimes the order of 2 meters (e.g. at $t = 1.5$ h).

The most striking error model difference resides in the orbit and clock error models. The KF uses a 1.8 m error model (for GPS), whereas the LSE uses the URA, which is 2.4 m for the healthiest satellites. To verify whether the orbit and clock errors are an important contributor to these differences, a third case was studied, using the same ARAIM LSE approach, but with $\sigma_{orb} = 1$ m. These results are represented with the orange curve in Figure 3. We can see that the covariance has dropped from the previously observed values, suggesting that σ_{orb} does have an important impact on the covariances observed here.

4. Sensitivity Analysis

In this section, we analyze the sensitivity of the KF to the choice of FOGMRP parameters (σ and τ), for each GNSS error. Each of the parameters described in Table 1 are modified one by one by 20% of their initial value. To look at worsening of the KF vertical position standard deviation, we increase the FOGRMP standard deviations and decrease the time constants by 20%. The vertical position covariance estimate resulting from this increase/decrease is denoted as σ_{inc}. These results are then individually compared to the "nominal KF" results (here denoted σ_{nom}) presented in previous sections.

The performance improvement metric used in this subsection is the following ratio:

$$q(t) = \frac{\sigma_{inc}(t)}{\sigma_{nom}(t)}. \tag{24}$$

In Figure 4, the curves in various shades of blue (squares) represents the evolution of the ratio q of Equation 24 when the FOGMRP parameters of the orbit and clock model are being modified (see red triangles and green circles curves for tropospheric and multipath models respectively). Curves above 1 correspond to results for which the 20% modification resulted in a larger covariance.

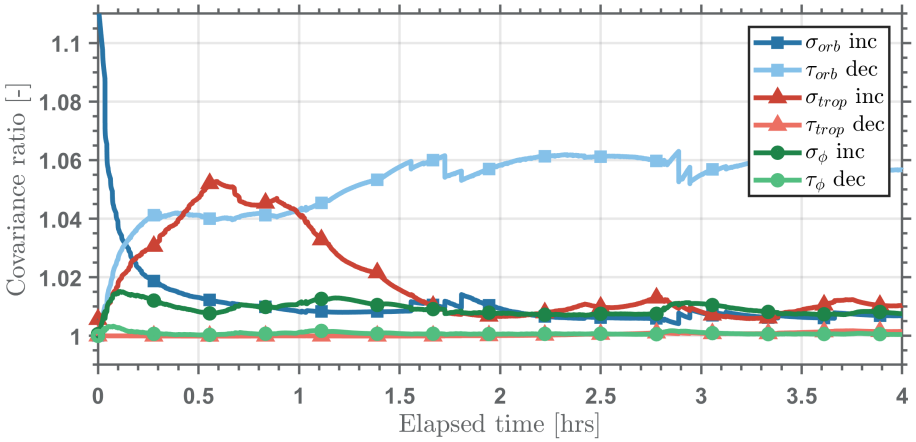

Figure 4: Sensitivity to the FOGMRP parameters

The orbit and clock error model seem to be the most sensitive of the 3 error types. Increasing its standard deviation σ_{orb} by 20% resulted in a 10% increase of the KF vertical position error standard deviation at $t = 0$ h. But this impact gets tapered as the KF converges (i.e. for $t > 30$ min), with an asymptotic ratio of about 1.1 (meaning a 1% increase in the KF output standard deviation). Of all the curve shown in this figure, the one representing a 20% decrease of the orbit and clock error time constant (light blue curve) is the one with the largest ratio after convergence, with a 6% increase in vertical position error standard deviation (i.e. $q = 1.06$). Further analysis revealed that this result was driven by the GPS constellation. At $t = 0$ h, the vertical position standard deviation is very large, and the same for both σ_{inc} and σ_{nom} of Equation 24. Both KFs start from the same very large value (ratio of 1) and filter data to converge to different values (since both time constants are now different).

Another large impact is observed with the tropospheric model (in particular its standard deviation parameter). Additional analysis revealed that the large ratio behavior observed at $t = 0.75$ h is geometry dependent and due to low elevation satellites getting in and out of view. One can notice that the satellite geometry impact on the KF output variance become negligible once the KF has converged: similar geometry variations are present at $t = 2.7$ h and $t = 3.7$ h, but these have no impact on q. One can also note that the 20% decrease of τ_{trop} has had no impact on the KF vertical position standard deviation. This is because a modification time constant from 20 to 16 hours will not be noticeable over a 4 hour KF run time.

Finally, the least impacting error model is the carrier phase multipath's, shown in green. Modifying the time constant proves to have a negligible impact on the KF vertical position standard deviation, and modifying its standard deviation resulted in a small 1% increase of the KF vertical position standard deviation.

The past 3 subsections analysed various aspects of the KF vertical position error standard deviations: how much lower they were compared to LSE's and how sensitive they were to their error models. These standard deviations must now be validated with data. The following subsection will do so over multiple data sets.

5. Overall performance of KF with time correlated bounding models

In this section, 6 consecutive data sets of 4 h each are processed into the KF described in Section IV. The state position estimate and its standard deviation estimate in the down direction are analysed. To validate (over a small sample of test data) the covariance results shown in previous subsection, Figure 5 represents the temporal evolution of the vertical position estimate ϵ_D, normalized by its associated standard deviation estimate σ_D. Each data set is represented in its own shade of blue, and the red area highlighted in the figure represents the area for which this ratio is smaller than 1. Also note that the inflation factor (Equation 23) on the cycle ambiguity covariance initialisation is set to 3 in order to account for the group delay impacting the raw code measurements during the cycle ambiguity initialization.

More than 67% (i.e. 1 sigma) of the data lays within the highlighted bounds, confirming that the models developed in prior work, and the KF implementation introduced here is valid. A more thorough analysis will be performed in future works over longer durations (i.e. more datasets). Increasing the number of data sets present in our analysis, would provide greater statistical confidence in those results.

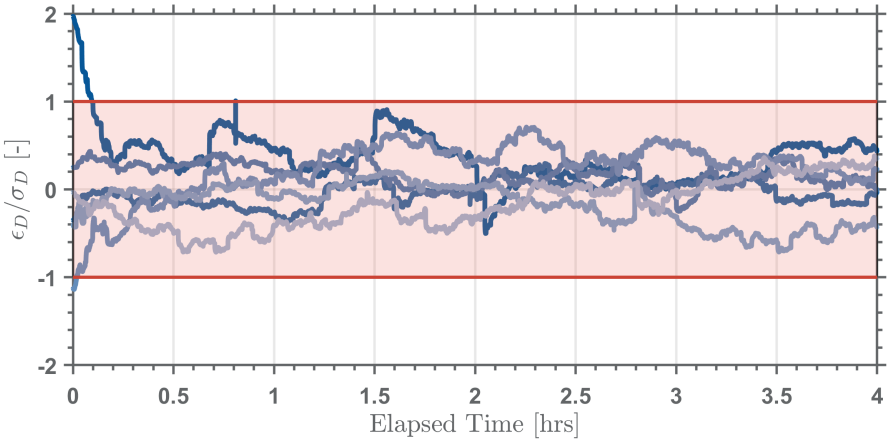

Figure 5: Covariance validation results over 6 sets of 4h

VI. CONCLUSION

Over the past few years, prior work has been done in the development of robust, time correlated error models for all three of the errors impacting iono-free GNSS measurements. These error models were put to the test in this paper, with real data and a Kalman Filter implementation.

With the same error models as input, the KF showed smoother and lower (after convergence) vertical position error standard deviations than its LSE counterpart. Additionally, the current ARAIM LSE implementation showed much larger and jagged standard deviations than when using the KF approach developed in this paper. A large part of their magnitude could be attributed to the orbit and clock error models currently in use in ARAIM.

The KF sensitivity to its FOGMRP error model was studied in turn. Results showed that increasing the time constant of any

of the FOGMRP models almost always resulted in a decreased KF vertical position error standard deviation output, whereas increasing the standard deviation of the models had the opposite effect. The KF standard deviations were shown to be very sensitive to orbit and clock error model modification, in particular their time constant.

Finally, one could note that the large vertical position error standard deviation decrease from the LSE ARAIM approach to the KF appraoch presented here could extend the scope of ARAIM to other applications with more stringent requirements, such as rail, harbor and arctic navigation.

Future work also needs to be performed by extending those results to a faulted scenario, in order to truly assess the performance of our KF and its error models under safety critical conditions.

ACKNOWLEDGEMENTS

The authors would like to thank the Federal Aviation Administration (FAA) for their support of this research. However, the opinions in this paper are our own and do not necessarily represent those of any other person or organization.

REFERENCES

Boehm, G., Moller, M., Schindelegger, M., Pain, G., and Weber, R. (2014). Development of an improved empirical model for slant delays in the troposphere (gpt2w). *GPS Solutions*, 19(1):433–441.

DeCleene, B. (2000). Defining pseudorange integrity overbounding. *Proceedings of the 13th International Technical Meeting of the Satellite Division of The Institute of Navigation (ION GPS 2000)*, pages 1916 – 1924.

Gallon, E., Joerger, M., Perea, S., and Pervan, B. (2019). Error model development for ARAIM exploiting satellite motion. *Proceedings of the 32nd International Technical Meeting of The Satellite Division of the Institute of Navigation (ION GNSS+ 2019)*, pages 3162–3174.

Gallon, E., Joerger, M., and Pervan, B. (2020). Frequency Domain Modeling of Orbit and Clock Errors for Sequential Positioning. *Proceedings of Institute of Navigation GNSS+ Virtual Conference (ION GNSS+ 2020)*, pages 1041 – 1053.

Gallon, E., Joerger, M., and Pervan, B. (2021). Robust modeling of gnss tropospheric delay dynamics. *IEEE Transactions on Aerospace and Electronic Systems*, 57(5):2992 – 3003.

Gallon, E., Joerger, M., and Pervan, B. (2022). Robust Modeling of GNSS Orbit and Clock Error Dynamics. *NAVIGATION: Journal of the Institute of Navigation*, pages 1–1.

Joerger, M. and Pervan, B. (2020). Multi-constellation ARAIM exploiting satellite motion. *NAVIGATION, Journal of the Institute of Navigation*, 67(2):235–253.

Langel, S. (2014). *Bounding estimation integrity risk for linear systems with structure stochastic modeling uncertainty*. PhD thesis, Illinois Institute of Technology.

Langel, S., García Crespillo, O., and Joerger, M. (2020). A new approach for modeling correlated gaussian errors using frequency domain overbounding. *2020 IEEE/ION Position, Location and Navigation Symposium (PLANS)*, pages 868–876.

Perea, S. D. (2019). *Design of an Integrity Support Message for Offline Advanced RAIM*. PhD thesis.

Rife, J., Pullen, S., Enge, P., and Pervan, B. (2006). Paired overbounding for nonideal LAAS and WAAS error distributions. *IEEE TAES*, 42(4):1386–1395.

Tanil, C., Khanafseh, S., Joerger, M., and Pervan, B. (2018). An INS monitor to detect GNSS spoofers capable of tracking vehicle position. *IEEE Transactions on Aerospace and Electronics*, 64(1):131–143.

Working Group C (2012). ARAIM Technical Subgroup. Interim Report Issue 1.0. Technical report, EU-US Cooperation on Satellite Navigation, N/A.

Working Group C (2014). ARAIM Technical Subgroup. Milestone 2.0 Report. Technical report, EU-US Cooperation on Satellite Navigation, N/A.

Working Group C (2016). ARAIM Technical Subgroup. Milestone 3.0 Report. Technical report, EU-US Cooperation on Satellite Navigation, N/A.